RSC Advances

PAPER

View Article Online
View Journal | View Issue

Cite this: *RSC Adv.*, 2021, **11**, 14399

Unique hierarchical SiO_2@$ZnIn_2S_4$ marigold flower like nanoheterostructure for solar hydrogen production†

Aarti R. Gunjal,[ab] Yogesh A. Sethi,[a] Ujjwala V. Kawade,[a] Rajendra P. Panmand,[c] Chitra K. Ugale,[a] Jalindar D. Ambekar,[b] Arvind V. Nagawade*[b] and Bharat B. Kale*[a]

The novel marigold flower like SiO_2@$ZnIn_2S_4$ nano-heterostructure was fabricated using an *in situ* hydrothermal method. The nanoheterostructure exhibits hexagonal structure with marigold flower like morphology. The porous marigold flower assembly was constructed using ultrathin nanosheets. Interestingly, the thickness of the nanopetal was observed to be 5–10 nm and tiny SiO_2 nanoparticles (5–7 nm) are decorated on the surface of the nanopetals. As the concentration of SiO_2 increases the deposition of SiO_2 nanoparticles on $ZnIn_2S_4$ nanopetals increases in the form of clusters. The optical study revealed that the band gap lies in the visible range of the solar spectrum. Using X-ray photoelectron spectroscopy (XPS), the chemical structure and valence states of the as-synthesized SiO_2@$ZnIn_2S_4$ nano-heterostructure were confirmed. The photocatalytic activities of the hierarchical SiO_2@$ZnIn_2S_4$ nano-heterostructure for hydrogen evolution from H_2S under natural sunlight have been investigated with regard to the band structure in the visible region. The 0.75% SiO_2@$ZnIn_2S_4$ showed a higher photocatalytic activity (6730 $\mu mol^{-1}\ h^{-1}\ g^{-1}$) for hydrogen production which is almost double that of pristine $ZnIn_2S_4$. Similarly, the hydrogen production from water splitting was observed to be 730 $\mu mol^{-1}\ h^{-1}\ g^{-1}$. The enhanced photocatalytic activity is attributed to the inhibition of charge carrier separation owing to the hierarchical morphology, heterojunction and crystallinity of the SiO_2@$ZnIn_2S_4$.

Received 10th February 2021
Accepted 10th April 2021

DOI: 10.1039/d1ra01140e

rsc.li/rsc-advances

1 Introduction

In recent years, the combined extreme energy shortages and environmental degradation have been triggered by technological development that demands a huge amount of fossil oil. Therefore, intensive studies focus on investigating alternative energy resources with renewable and environmentally-friendly advantages.[1,2] Among them, hydrogen will be considered a possible candidate for future use in conventional fuels.[3] Photocatalytic H_2S & water splitting is one of the most promising approaches for hydrogen production, as it can perform a conversion that converts solar light into chemical energy.[4–6] Various materials with important photocatalytic hydrogen evolution properties, such as MoS_2, $BiVO_4$, CuO, Ti_3C_2 *etc.*, have been prepared to date.[7–10] Ternary $ZnIn_2S_4$ is a semiconductor chalcogenide with great visible-light-responsive photocatalytic activity, considerable chemical stability and ample flat band potential which attracted considerable interest in lithium ion batteries and gas sensor applications.[11–15]

As one of the most promising n-type semiconductors, $ZnIn_2S_4$ has captured much interest in the field of photocatalytic hydrogen generation, which can be attributed to its non-toxic properties and suitable band structure (2.2–2.5 eV)[16,17] Similar to other photocatalysts, $ZnIn_2S_4$ suffers electron–hole recombination, slow oxygen evolution reaction kinetics and low visible light utilization.[18] Combining $ZnIn_2S_4$ with other semiconductors is an effective method to inhibit the recombination of photogenerated charge carriers and improve the photocatalytic activity. Until now, many $ZnIn_2S_4$ nanoheterostructures and doped $ZnIn_2S_4$ with various morphologies such as $ZnIn_2S_4$/$Ni_{12}P_5$,[19] g-C_3N_4/Ag:$ZnIn_2S_4$,[20] SnS@$ZnIn_2S_4$,[21] Ag-doped $ZnIn_2S_4$,[22] CdS/QDs/$ZnIn_2S_4$,[23] Ti_3C_2 MXene@TiO_2/$ZnIn_2S_4$ (ref. 24) have been reported to exhibit admirable visible-light photocatalytic activity. These literatures emphasized that while some prodigious work has been done in the field of photocatalysis, catalytic efficiency is still insufficient. It also needs more studies to explore new ways of further improving it.

SiO_2 is an insulator mesoporous material. SiO_2 has been widely used in the fields of catalysis, separation and adsorption due to its large specific surface area, abundant surface hydroxyl

[a]Dr John Barnabas post-graduate School for Biological Studies, Ahmednagar College, Ahmednagar, India. E-mail: avnagawade@gmail.com

[b]Nanocrystalline Laboratory, Centre for Material for Electronic Technology (CMET), Department of Information Technology, Govt. of India, Panchawati, Off Pashan Road, Pune 411007, India. E-mail: bbkale1@gmail.com; bbkale@cmet.gov.in; Fax: +91 20 2589 8180; Tel: +91 20 2589 9273

[c]Microwave Materials Division, Centre for Material for Electronic Technology (CMET), Shoranur Road, Athani, Thrissur-680 581, India

† Electronic supplementary information (ESI) available. See DOI: 10.1039/d1ra01140e

groups, environmental friendliness, stable chemical properties, uniform pore size and relatively high mechanical strength.[25–27] SiO_2 is mainly used in many heterostructures to enhance the photocatalytic performance of other semiconductor by increasing the surface area of the catalyst and it affects on the charge carrier recombination.[28,29] In past, various attempts have been made to enhance the photocatalytic activity of individual semiconductors by coupling with SiO_2 such as g-C_3N_4/SiO_2,[30] SiO_2@TiO_2core@Shell,[31] SiO_2/CNOs/TiO_2,[32] g$C3N_4$/TiO_2/Fe_3O_4@SiO_2,[33] γ-Fe_2O_3@SiO_2@TiO_2,[34] TiO_2–SiO_2Ag,[35] NiO/SiO_2,[36] $ZnFe_2O_4$@SiO_2@TiO_2.[37] So, to overcome the problem of fast recombination of photoinduced electron–hole pair and enhance the photocatalytic performance of pure $ZnIn_2S_4$, we synthesized a $ZnIn_2S_4$ and decorated with SiO_2 nanoparticles to enhance the separation and transfer efficiency of electrons. With this motivation, we have prepared a new SiO_2@$ZnIn_2S_4$ hybrid semiconductor by coupling SiO_2 and $ZnIn_2S_4$. To the best of our knowledge, this is the first report on SiO_2@$ZnIn_2S_4$ heterostructure for H_2 production from H_2S & Water splitting.

In the view of above findings, we report the hierarchical SiO_2@$ZnIn_2S_4$ nano-heterostructure for efficient generation of hydrogen, which was synthesized using facile hydrothermal method. These fabricated heterostructures were thoroughly characterized using XRD, FESEM, UV-Vis spectroscopy, PL and TEM. The fabrication of SiO_2@$ZnIn_2S_4$ nano-heterostructure increases the charge separation and also enhances the solar light response. Thus, under solar light irradiation, the high output rate of hydrogen is observed. In addition, the component effect on photocatalytic efficiency of SiO_2@$ZnIn_2S_4$ nano-heterostructure and the proposed photocatalytic mechanism have been further investigated.

2 Experimental sections

Zinc nitrate hexahydrate ($Zn(NO_3)_2 \cdot 6H_2O$), Indium nitrate ($In(NO_3)_3 \cdot 4H_2O$), Thiourea ($CSNH_2CS$),Silicon Dioxide (SiO_2) used for the preparation of catalysts are of analytical grade (SD-fine-chem limited, India) and used without any further purification.

2.1 Synthesis of $ZnIn_2S_4$ and SiO_2@$ZnIn_2S_4$

All the chemicals used for SiO_2@$ZnIn_2S_4$ synthesis were analytical grade and used without further purification. The hydrothermal method was used to synthesise SiO_2@$ZnIn_2S_4$ photocatalysts and the procedure is briefly defined as follows: first, 1 mole of hexahydrate zinc nitrate ($Zn(NO_3)_2 \cdot 6H_2O$) (99.99%) and 2 moles of indium nitrate ($In(NO_3)_3 \cdot 4H_2O$) (99.99%) and 8 moles of thiourea were mixed in a beaker (a) in 70 mL distilled water and stirred at room temperature for 15 minutes. After stirring, 0.25 wt% of silicon dioxide was applied to the above solution in beaker (a). The clear solution was then moved to a Teflon autoclave with a capacity of 150 mL and held in an electric oven at 150 °C for 30 hours. As the synthetic catalyst was washed several times with absolute ethanol and deionized water, the yellow powder was obtained. For pure $ZnIn_2S_4$, 0.25%SiO_2@$ZnIn_2S_4$, 0.50%SiO_2@$ZnIn_2S_4$, 0.75% SiO_2@$ZnIn_2S_4$, 1% SiO_2@$ZnIn_2S_4$ were labelled as (ZS-1), (ZS-2), (ZS-3), (ZS-4) and as (ZS-5) respectively and were subsequently used for further analysis and comparison.

2.2 Photocatalytic study

2.2.1 Photocatalytic hydrogen generation from water. The photochemical reaction was carried in a 70 mL total volume air-tight cylindrical quartz reactor with a cooling jacket for water circulation. All the reactions were carried out at ambient conditions under natural sunlight on sunny days (March to May months) between 10 am to 3 pm at Pune, located in the Maharashtra state of India. The intensity of solar light was measured by using a digital Lux meter. The measured average intensity of solar light reaching the surface of the earth was 145 000 Lux. In a typical photocatalytic experiment, 15 mg of the photocatalyst was dispersed in 25 mL total volume containing 20% methanol (v/v) in aqueous solution. The 45 mL free space of photoreactor made airtight with rubber septum followed by ultrasonication for 5 min for the uniform dispersion of catalyst. The solution mixture was then purged with Ultra High Purity nitrogen gas (UHP-99.999%) to remove all the gases in the headspace of the reactor and dissolved oxygen from the reaction mixture. Before and after irradiation with solar light, the gas in the free space of the reactor was analyzed using gas chromatography (GC). The generated gas was analyzed immediately using GC with a specific time interval.

2.2.2 Photocatalytic hydrogen generation from water. The hydrogen generation is performed in a cylindrical quartz photochemical thermostatic reactor introducing 0.5 g SiO_2@-$ZnIn_2S_4$. The reactor was filled with 700 mL 0.5 M aqueous KOH and purged with Argon for 30 min. Hydrogen sulfide is bubbled through the solution for 1 h at the rate of 2.5 mL min^{-1} at 299 K. SiO_2@$ZnIn_2S_4$ photocatalyst is introduced as a suspension into a cylindrical quartz reactor and irradiated with the sunlight at a constant stirring with a continuous flow of H_2S (2.5 mL min^{-1}). The excess of H_2S was trapped in 10% NaOH solution. The amount of H_2 gas evolved was measured using a graduated gas burette and analyzed using gas chromatography technique (GC) equipped with thermal conductivity detector (TCD) and Porapak-Q packed column with N_2 as a carrier gas.

2.3 Samples characterization

The phase formation and crystallite size of all synthesized samples were estimated *via* X-ray Diffractometry (XRD-D8, Advance, Bruker-AXS) with Ni-filtered Cu-Kα radiation (λ = 1.5418 Å). Optical properties of the bare and Au loaded samples were studied by UV-Vis-DRS spectrophotometer (UV 2600 spectrometer, Lambda-950, Perkin-Elmer) in the spectral range of 200–800 nm. The surface morphology was characterized using Field Emission Scanning Electron Microscopy (FESEM; Hitachi, S-4800 II) and Field Emission Transmission Electron Microscopy (FETEM; JEM-2000 FS). Image processing and interplanar distance (d) evaluation were performed with the help of micrograph Gatan software. Surface characterization of all SiO_2@$ZnIn_2S_4$ samples was carried out using X-ray

Photoelectron Spectroscopy (XPS, ESCA3000, VG Scientific Ltd.) at a pressure of >1 × 10–9 Torr. The general scan C1s, S2p, In3d, Sn3d, and Zn2p core level spectra were recorded with non-mono chromatized Mg-Kα radiation (photon energy-1253.6 eV). Baseline correction and peak fitting for all the samples were done using software package XPS peak-41. The core level binding energies (BEs) were aligned with respect to the C1s binding energy of 285 eV. The collected gas sample was analyzed using a Gas chromatography system (Shimadzu GC-2014) with portapak-Q packed column coupled with TCD detector and nitrogen (N2-UHP) as a carrier gas.

3 Results and discussions

3.1 Structural study

The phase purity and crystallinity of the as-synthesized pristine $ZnIn_2S_4$ and SiO_2@$ZnIn_2S_4$ nano-heterostructure were investigated by using X-ray diffraction analysis. Fig. 1 depicts the XRD diffractogram of the as-synthesized samples (ZS1–ZS5). The pristine $ZnIn_2S_4$ (ZS1) shows diffraction peaks at 27.93°, 47.57°, 33.62°, 44.44°, 29.14° and 56.89° are indexed to crystalline planes (311), (440), (400), (511), (222), and (533), respectively. The diffraction peaks reveal presence of cubic phase of $ZnIn_2S_4$ (JCPDS 00-023-0295).[38] For the SiO_2@$ZnIn_2S_4$ nano-heterostructures, it has the similar XRD patterns like pristine $ZnIn_2S_4$ and the diffraction peaks corresponding to SiO_2 are not observed because very small amount of SiO_2 (*i.e.* less than equal to 1%).This also could be because of nano tiny SiO_2 surface is covered with dense nano-petals of $ZnIn_2S_4$, which may prevent XRD from detecting the inner SiO_2. Additionally, the peak intensity of $ZnIn_2S_4$ slightly decreased with the increase of SiO_2 content. The crystalite size is obtained for nanoheterostructure is around 15 nm against bare $ZnIn_2S_4$ *i.e.* 13.65 nm. The lattice parameter of SiO_2@$ZnIn_2S_4$ is $a = b = c$ 10.78 Å having cubic system (space group *Fd3m* & space group number 227). The XRD findings may suggest the coexistence of SiO_2 and $ZnIn_2S_4$ in the nano-heterostructures of SiO_2@$ZnIn_2S_4$, which will be further illustrated by the following observations from XPS, FESEM and TEM. No diffraction peaks were obtained for any impurities, which indicate the pure nature of the SiO_2@$ZnIn_2S_4$ samples as-synthesised.

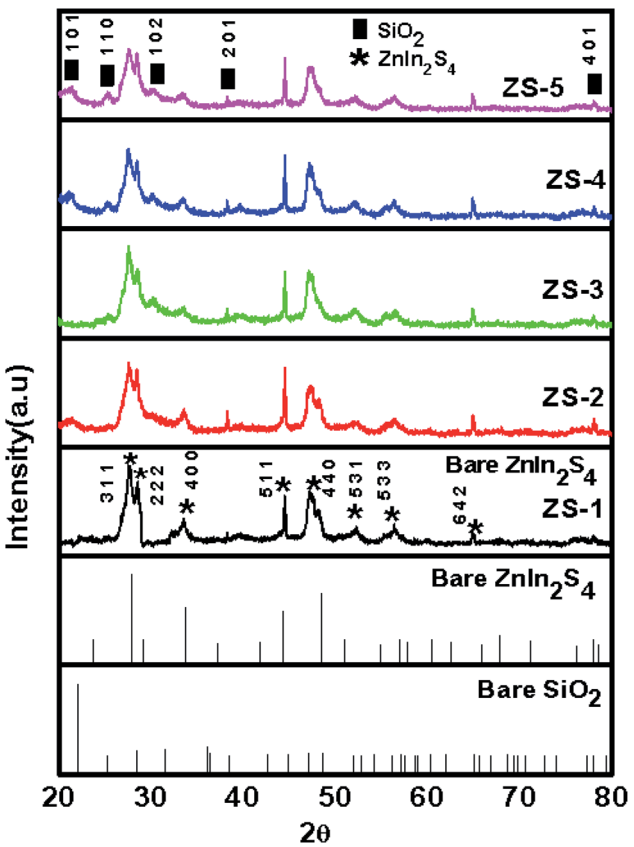

Fig. 1 X-ray diffraction patterns of (ZS1) pure $ZnIn_2S_4$ (ZS2) 0.25% SiO_2@$ZnIn_2S_4$ (ZS3) 0.50% SiO_2@ZnIn2S4 (ZS4) 0.75% SiO_2@$ZnIn_2S4$ and (ZS5) 1% SiO_2@$ZnIn_2S_4$ sample Photocatalyst.

3.2 Surface and morphological studies

The morphological investigation of as-synthesized SiO_2@-$ZnIn_2S_4$ nano-heterostructures was observed by using field emission scanning electron microscopy (FESEM). Fig. 2 shows FESEM images of as-synthesized pristine $ZnIn_2S_4$ (ZS1) and SiO_2@$ZnIn_2S_4$ (ZS2–ZS5) nano-heterostructures. The low magnification image (Fig. 2a) of pristine $ZnIn_2S_4$ demonstrates the ultrathin curled nanosheets which self-assembled in the form of marigold flower. The average diameter of flower was found to be 7–12 um. The high magnification image (Fig. 2b) indicate that these flower are assembled by ultrathin interlocked nanosheets (nanopetal) with the thickness about 5–10 nm. The FESEM images of SiO_2@$ZnIn_2S_4$ nano-heterostructures (ZS-2 to ZS-5) as shown in Figure (2c to j). From figures, the effect of addition of SiO_2 on surface morphologies of nano-heterostructures was investigated.

Fig. 2c–j depicts FESEM imagos of as-synthesized nano-heterostructures (ZS-2 to ZS-5), where the flowers like morphology was retained. Most significantly, extremely crystalline ultrathin nanosheets are seen in case of ZS-4 (Fig. 2g and h). This shows the fully grown ultrathin nanosheets curled and form nanoflowers. Furthermore, as percentage of SiO_2 increases (ZS-5), the small SiO_2 nanoparticles deposited on nanopetals of flower & ultrathin nanosheets (nanopetals) get distorted (Fig. 2i and j). As the concentration of SiO_2 increases there is a deposition of the SiO_2 particles on the nanopetals of $ZnIn_2S_4$. Further, increasing concentration, there is a formation of SiO_2 clusters on nanopetal of the flowers. We observed uniform deposition/coating for sample ZS-4 (Deposition of 0.75% SiO_2).

The microstructural aspects of as-synthesized SiO_2@$ZnIn_2S_4$ (ZS-4) nano-heterostructure were confirmed by field emission transmittance electron microscopy (FETEM). Fig. 3 depicts the TEM images of SiO_2@$ZnIn_2S_4$. The TEM images of SiO_2@-$ZnIn_2S_4$ clearly shows flower-like structure formed by ultrathin nanosheets (nanopetals). These results are well in accordance with FESEM (Fig. 2). More specific details about the nano-heterostructure of SiO_2@$ZnIn_2S_4$ was further examined by HRTEM, as shown in Fig. 3c. The lattice fringes are distinctly identified with interplanar distances of 0.312 nm and 0.4 nm,

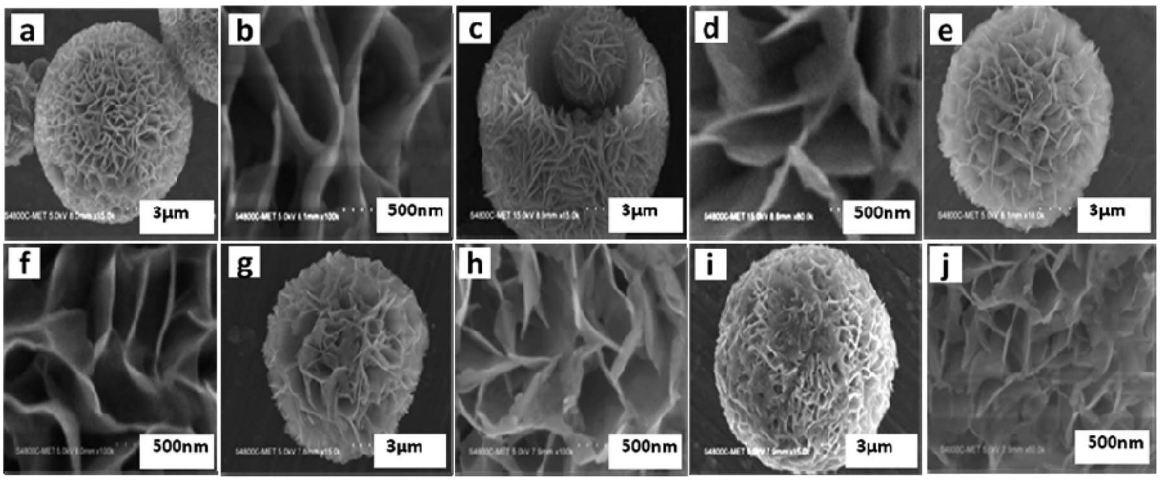

Fig. 2 Representative FE-SEM images of (a and b) pure $ZnIn_2S_4$ (c and d) 0.25% SiO_2@$ZnIn_2S_4$ (e and f) 0.50% SiO_2@$ZnIn_2S_4$ (g and h) 0.75% SiO_2@$ZnIn_2S_4$ and (i and j) 1% SiO_2@$ZnIn_2S_4$ sample photocatalyst.

which correlates to the *d* spacing of (311) and (101) planes of $ZnIn_2S_4$ and SiO_2, respectively.[39,40] Fig. 3d demonstrate the selected area diffraction pattern of as-synthesized sample, which clearly shows polycrystalline nature of SiO_2@$ZnIn_2S_4$ nano-heterostructure. From Fig. 3e, the observed diffraction dots can be assigned to (311) and (101) planes of $ZnIn_2S_4$ and SiO_2, respectively. These results are consistent with XRD results. To investigate the distribution of SiO_2 in SiO_2@$ZnIn_2S_4$ nano-heterostructure the EDS analysis was performed (Fig. 3e and f). These results clearly indicate the uniform distribution of Si,

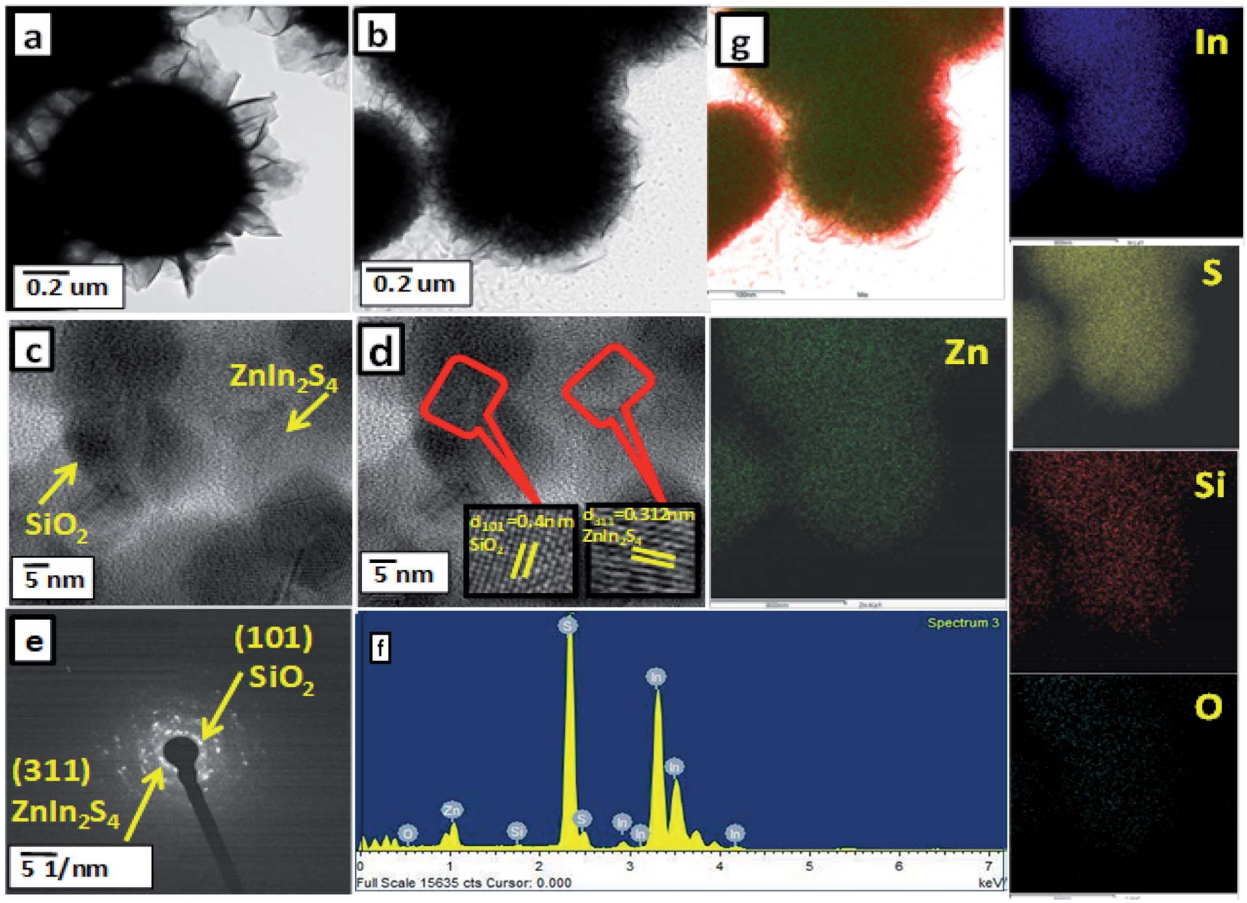

Fig. 3 (a) FE-TEM images of pure $ZnIn_2S_4$, (b) FE-TEM images of SiO_2@$ZnIn_2S_4$, (c) HRTEM (d) SAED pattern (e) EDAX spectra and (f) elemental mapping of 2% SiO_2 loaded $ZnIn_2S_4$.

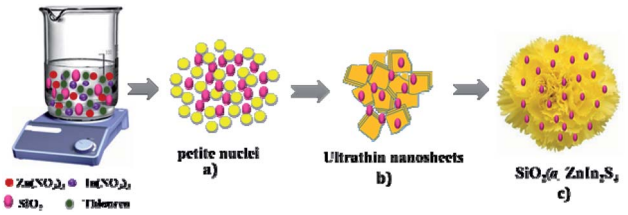

Scheme 1 Schematic representation of the formation mechanism of SiO_2@$ZnIn_2S_4$ nanoheterostructure.

Zn, In, S, & O in SiO_2@$ZnIn_2S_4$ nano-heterostructure. More significantly, the TEM results confirm the successful formation of SiO_2@$ZnIn_2S_4$ nano-heterostructure and there exists intimate contact between SiO_2 and $ZnIn_2S_4$.

We can easily predict the mechanism of the flower-like structure of SiO_2@$ZnIn_2S_4$ based on morphological studies. Initially, the nucleation begins to form the Zn^{2+}, In^{3+} and S^{2-} ions with the dissociation of the sulphur source, zinc and indium nitrate precursor at a low temperature. The degree of dissociation of zinc and indium salts is greater in the water-like polar solvent. In the supersaturated solution, the petite nuclei were formed and there was further growth of nanoparticles over a time (Scheme 1). In order to minimize their surface energy that further evolves anisotropically along with 2D directions, these new nanoparticles impulsively agglomerated, aligned and confer the formation of ultra-thin nanosheets (Nanopetals). And then after prolonged hydrothermal reaction the curled nanopetals are formed because of surface tension created on the petals. Further, this curving nature petals self-assembled and form marigold like flower structure. During reaction the disperse SiO_2 nanoparticles gets deposited on the surface of the nanopetals.

3.3 Optical properties

The optical absorption study of the pristine $ZnIn_2S_4$ and SiO_2@$ZnIn_2S_4$ nano-heterostructures is important for its photocatalytic application. The UV-Vis diffuse reflectance spectra of as-synthesized nano-heterostructures (ZS-1 to ZS-5) are shown in the Fig. 4. The $ZnIn_2S_4$ shows an absorption edge of about 570 nm and its band gap is estimated to be 2.16 eV.[41] Compared to the pristine $ZnIn_2S_4$, the all SiO_2@$ZnIn_2S_4$ nano-heterostructures exhibited a small red shift in UV-vis diffuse reflectance absorption spectrum (DRS) and the visible light absorption intensity was also increased due to SiO_2 nanoparticles decoration. The addition of SiO_2 will greatly improve light harvesting, separation and transfer of photoinduced charge carriers (h^+/e^-) and can be shown by the following spectrum of photoluminescence. Thus, SiO_2@$ZnIn_2S_4$ nano-heterostructures demonstrated promising usage as a photocatalyst under visible light irradiation relative to pristine $ZnIn_2S_4$.

Photoluminescence (PL) emission spectrum measurement was performed for pristine $ZnIn_2S_4$ (ZS1) and SiO_2@$ZnIn_2S_4$ (ZS2–ZS5) nano-heterostructures (Fig. 5). This spectrum can provide useful information on capture and recombination charge carriers in semiconductor. The ZS-1 PL spectrum displays a broad peak ~572 nm, attributing to the band gap transfer emission with the light energy nearly equivalent to the $ZnIn_2S_4$ band gap energy.[42] For SiO_2@$ZnIn_2S_4$ Samples, their PL spectra are similar to that of pristine $ZnIn_2S_4$, but after SiO_2 modification a significant decrease in PL intensity was observed. Such obvious reduction in PL intensity strength revealed the suppression in recombination rate of photogenerated e^- & h^+ in the SiO_2@$ZnIn_2S_4$. Interestingly, ZS-4 has shown lowest PL Intensity which indicates optimum concentration of SiO_2 can inhibit electron hole recombination strongly. At very high concentration of SiO_2 *i.e.* 1% the transport of electrons get hindered which ultimately increased the electron hole recombination. However, at moderate SiO_2 concentration *i.e.* 0.75% to electron transport to the surface is quite high. Therefore, we conclude that of the ZS-4 sample has more efficient charge carrier separation compared to other samples.[43]

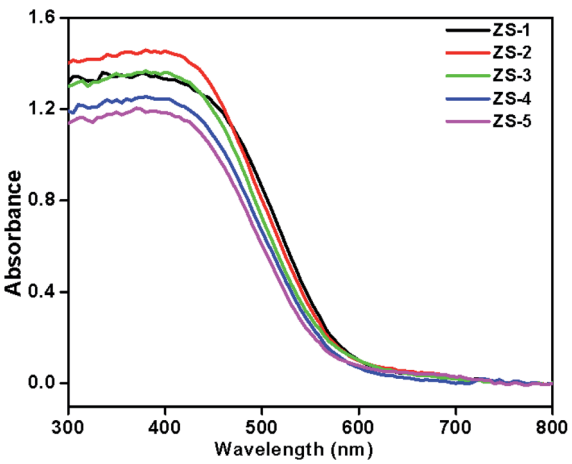

Fig. 4 UV-DRS spectra of (ZS1) pure $ZnIn_2S_4$ (ZS2) 0.25% SiO_2@-$ZnIn_2S_4$ (ZS3) 0.50% SiO_2@$ZnIn_2S_4$ (ZS4) 0.75% SiO_2@$ZnIn_2S_4$ and (ZS5) 1% SiO_2@$ZnIn_2S_4$ sample photocatalyst.

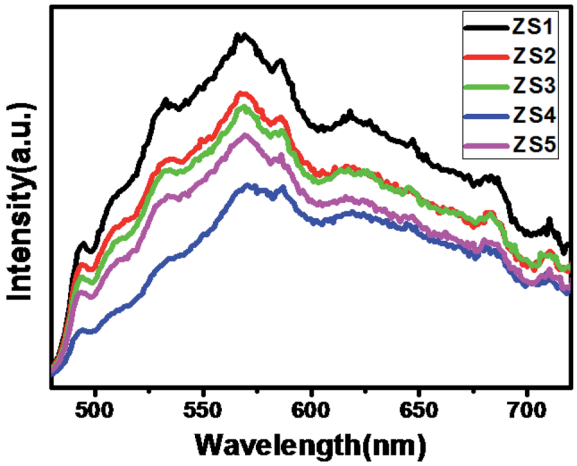

Fig. 5 Photoluminescence spectra of (ZS1) pure $ZnIn_2S_4$ (ZS2) 0.25% SiO_2@$ZnIn_2S_4$ (ZS3) 0.50% SiO_2@$ZnIn_2S_4$ (ZS4) 0.75% SiO_2@$ZnIn_2S_4$ and (ZS5) 1% SiO_2@$ZnIn_2S_4$ sample photocatalyst.

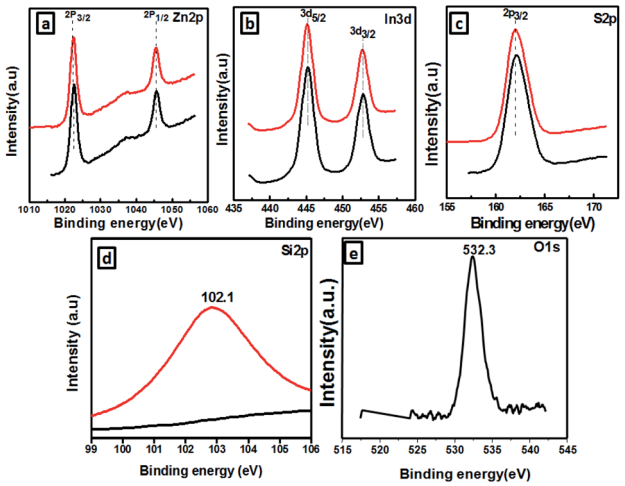

Fig. 6 XPS spectra of the as-prepared SiO_2@$ZnIn_2S_4$ (a) Zn2p, (b) In3d, (c) S2p, (d) Si3d.

3.4 XPS study

The SiO_2@$ZnIn_2S_4$ XPS spectra are analyzed in a contrastive manner in order to further confirm the formation of the SiO_2@$ZnIn_2S_4$ nano-heterostructure and determine its elemental composition and valence states. The Zn 2p, In 3d, S 2p, Si 2P, and O 1 s high-resolution XPS spectra provides more detailed information on the chemical state of these elements in Fig. 6a–e respectively. Fig. 6a shows the Zn 2p region in SiO_2@$ZnIn_2S_4$ nano-heterostructure with high resolution. Based on figure, $2p_{1/2}$ and $2p_{3/2}$ splitting respectively defined the doublet of Zn 2p. The binding energies at 1046.02 eV associated with Zn^{2+} $p_{1/2}$, whereas those of 1021.24 eV were correlated with Zn^{2+} $p_{3/2}$.[44] Fig. 6b shows the In 3d high-resolution spectrum and the SiO_2@$ZnIn_2S_4$ nano-heterostructure peak at 453.54 eV and 445.18 eV corresponds to In^{3+} $3d_{3/2}$ and In^{3+} $3d_{5/2}$ respectively.[21] Furthermore, the XPS signal (Fig. 6c) observed at a 162.89 eV binding energy is attributed to S^{2-} $2p_{3/2}$ which is inconsistent with $ZnIn_2S_4$ results.[45] Similarly, Fig. 6d and e shows the high resolution spectrum of the energy levels of Si 2P and O 1 s. The binding energies located at 102.1 eV and 532.3 eV verified the existence of Si & O element in SiO_2@$ZnIn_2S_4$ nano-heterostructure.[46] On the basis of the above results, it indicates that SiO_2 nanoparticle are distributed uniformly on $ZnIn_2S_4$. Together with the TEM and optical results, these results suggest that $ZnIn_2S_4$ was hybridized with SiO_2 by the successful formation of nano-heterostructure, which provides synergistic interaction between SiO_2 and $ZnIn_2S_4$ matrices for the transfer of charge carriers.

3.5 Photocatalytic study

3.5.1 Photocatalytic activity measurement. As conferred earlier, SiO_2@$ZnIn_2S_4$ is a good semiconductor having a narrow band gap falling in the visible region at room temperature. Considering the good response towards solar light, photocatalytic activities of SiO_2@$ZnIn_2S_4$ have been investigated. Herein, we report the photocatalytic H_2 evolution performance from water and H_2S under natural sun light.

3.5.2 Photocatalytic H_2 evolution from H_2O. The effect of SiO_2 loading on $ZnIn_2S_4$ and their photo-catalytic activity of hydrogen generation were studied under natural sunlight irradiation using $Na_2S/Na_2S_2O_3$ as a scavenger electron donor. A series of experiments were performed using different concentrations of SiO_2 on the surface of $ZnIn_2S_4$, and their results are given in Table 1. The investigation results indicated that the maximum hydrogen generation, *i.e.* 796 μmol h^{-1} g^{-1}, was obtained for the sample ZS-4, whereas pure $ZnIn_2S_4$, shows hydrogen evolution rates of 138 μmol h^{-1} g^{-1}. Furthermore, 0.25% SiO_2@$ZnIn_2S_4$, 0.50% SiO_2@$ZnIn_2S_4$ & 1% SiO_2@$ZnIn_2S_4$ give 237, 480 & 643 μmol h^{-1} g^{-1} respectively from water splitting. Fig. 7 shows the time-dependent hydrogen generation

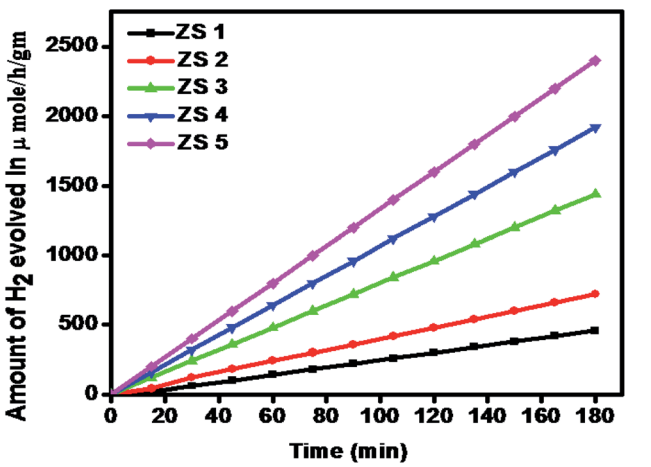

Fig. 7 Time *versus* volume of H_2 (μmole) evolution from H_2O of the all samples synthesized at (ZS-1) pure $ZnIn_2S_4$ and SiO_2@$ZnIn_2S_4$ nano-heterostructure prepared with a different percent of SiO_2 loading (ZS-2) 0.25%, (ZS-3) 0.50%, (ZS-4) 0.75%, and (ZS-5) 1%.

Table 1 The H_2 generation rates for as-synthesized $ZnIn_2S_4$, SiO_2 & SiO_2@$ZnIn_2S_4$

Sr. no.	Sample code	H_2 evolution rate from water (μmol h^{-1} g^{-1})	H_2 evolution rate from H_2S (μmol h^{-1} g^{-1})
1	ZS1	138	3350
2	ZS2	237	4320
3	ZS3	480	5650
4	ZS4	796	6730
5	ZS5	643	6050

using the as-synthesized $ZnIn_2S_4$ and SiO_2@$ZnIn_2S_4$ nano-heterostructures. The linearity of the graph shows a continuous and stable hydrogen generation rate. Which reveals that most exciting electrons are available for proton reduction. For this experiment, we used 70 mL DI water and $Na_2S/Na_2S_2O_3$ mixture as a sacrificial agent. In the present case, 0.25 M Na_2S and 0.35 M $Na_2S_2O_3$ mixture were used to resist the photo-corrosion of the semiconductor. Moreover, the Na_2S solution acts as a hole scavenger, and it oxidized S^{2-} into S^{2-}, which is beneficial for hydrogen generation from SiO_2@$ZnIn_2S_4$ rather than alcohol. The photocatalytic hydrogen generation mechanism from water is well reported and discussed in the previous literature.[47] The Semiconductor photocatalyst after interaction with solar light with energy greater than or equal to band gap energy generates electrons in CB and holes in VB. It causes redox reactions of adsorbed species on a semiconducting material. The photogenerated holes from VB irreversibly oxidize S^{2-}, which was reduced back to S^{2-} by $Na_2S_2O_3$ and radially got adsorbed on the surface of semiconductor producing protons (H^+) and free radicals, while electrons from CB reduce H^+ ions into molecular hydrogen.

$$SiO_2@ZnIn_2S_4 \xrightarrow{h\nu} e^- + h^+ \quad (1)$$

Oxidation:

$$SO_3^{2-} + 2OH^- + 2h^+ \rightarrow SO_4^{2-} + 2H^+ \quad (2)$$

$$2S^{2-} + 2h^+ \rightarrow S_2^{2-} \quad (3)$$

$$S_2^{2-} + SO_3^{2-} \rightarrow S_2O_3^{2-} + S^{2-} \quad (4)$$

$$SO_3^{2-} + S^{2-} + 2h^+ \rightarrow S_2O_3^{2-} \quad (5)$$

Reduction:

$$H^+ + 2e^- \rightarrow H_2 \quad (6)$$

3.7.1 Photocatalytic H2 evolution from H_2S splitting. The photocatalytic activity of the as-synthesized pristine $ZnIn_2S_4$ and SiO_2@$ZnIn_2S_4$ nano-heterostructure is evaluated for hydrogen production *via*. H_2S splitting under natural sunlight. Fig. 8 and Table 1 shows amount of hydrogen evolved *via*. H_2S splitting using ZS-1 to ZS-5 samples. The graph linearity clearly shows stable evolution rate of hydrogen. Control experiments indicated that no evolution of hydrogen was detected in the absence of photocatalyst.

From Fig. 8, it is observed that pristine $ZnIn_2S_4$ exhibits hydrogen production rate of 3350 μmol h^{-1} g^{-1}, The enhanced photocatalytic H_2 generation can be attributed to the hydrothermal assisted growth of flower-like $ZnIn_2S_4$ assembled from ultrathin nanosheets (nanopetals) which facilitates more catalyst surface for reaction and light harvesting. The photocatalytic hydrogen production activity of SiO_2@$ZnIn_2S_4$ nano-heterostructure increases with increase in SiO_2 content. The sample ZS-2 exhibits significant H_2 production rate 4320 μmol

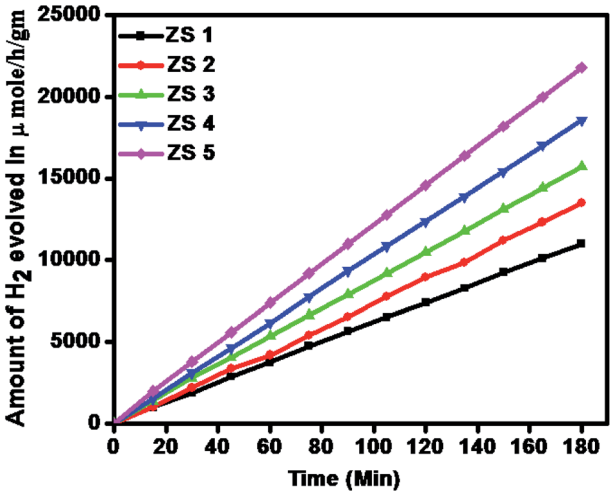

Fig. 8 Time *versus* volume of H_2 (μmole) evolution from H_2S of the all samples (ZS-1) pure $ZnIn_2S_4$ and SiO_2@$ZnIn_2S_4$ nanoheterostructure prepared with a different percent of SiO_2 loading (ZS-2) 0.25%, (ZS-3) 0.50%, (ZS-4) 0.75%, and (ZS-5) 1%.

h^{-1} g^{-1}, which is 30% higher compared to the ZS1 sample. Amongst all of the photocatalysts (ZS1–ZS5), 0.75 wt% loaded SiO_2@$ZnIn_2S_4$ nano-heterostructure (ZS-4) showed the highest rate for H_2 production (6730 μmol h^{-1} g^{-1}) under natural sunlight. The optimized 0.75 wt% loaded SiO_2@$ZnIn_2S_4$ shows twice hydrogen production rate as compared to pristine $ZnIn_2S_4$. The highest H_2 evolution was achieved for ZS-4 (0.75 wt% loaded SiO_2@$ZnIn_2S_4$) and is due to the high crystallinity, flower like morphology and band structure of SiO_2@-$ZnIn_2S_4$. More specifically, in contrast to earlier studies, the H_2 evolution obtained for sample ZS-4 is much greater. The sample ZS-5 shows substantially less evolution of H_2 due to the increase in band gap relative to sample ZS-4. It is mainly due to the fact that the relatively high weight ratio of SiO_2 in SiO_2@$ZnIn_2S_4$ (ZS-5) can increase shielding in the light absorption and opacity, which ultimately reduce penetration of light through the depth of the reaction solution. The efficient charge separation and possible hydrogen production mechanism in SiO_2@$ZnIn_2S_4$ nano-heterostructure explained by considering the SiO_2@-$ZnIn_2S_4$ band gap energy diagram as shown in Scheme 2. Initially, the nano-heterostructure SiO_2@$ZnIn_2S_4$ is irradiated under sunlight during photocatalysis. The photo-excitation of the charge carriers occurs in $ZnIn_2S_4$, which induces h^+ in the valence band (VB) and e^- in the $ZnIn_2S_4$ conduction band (CB). The photo-induced holes in the VB oxidizes S_2^{2-}/SO_3^{2-} to oxidation products ($SO_4^{2-}/S_2O_3^{2-}$).[48] Meanwhile, photo-induced electrons in the CB will move to the deposited SiO_2 nanoparticles in order to reduce H^+ to H_2.

$$H_2S + OH^- \leftrightarrow HS^- + H_2O \quad (7)$$

$$H_2S + OH^- \leftrightarrow S^{2-} + H_2O \quad (8)$$

$$\text{Photo catalyst} \rightarrow e_{CB}^- + h_{VB}^+ \quad (9)$$

$$2S^{2-} + 2\,h_{VB}^+ \rightarrow S_2^{2-} \quad (10)$$

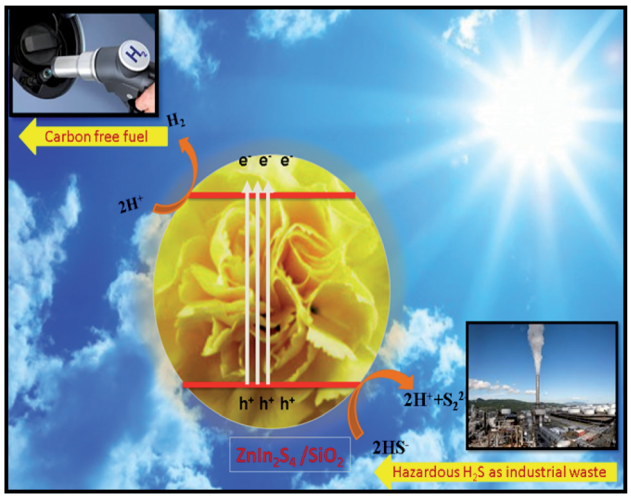

Scheme 2 Schematic representation of the photocatalytic mechanism of SiO_2@$ZnIn_2S_4$ heterostructure.

$$2HS^- + 2h_{VB}^+ \rightarrow S_2^{2-} + 2H^+ \quad (11)$$

$$2H^+ + 2e_{CB}^- \rightarrow H_2 \quad (12)$$

The existence of SiO_2 nanoparticles in SiO_2@$ZnIn_2S_4$ nanoheterostructure will thus prevent direct charge recombination and promote the separation of electrons and holes. Additionally, provide more active sites for surface reactions, resulting in the enhanced photocatalytic H_2 production using SiO_2@-$ZnIn_2S_4$. The enhancement of hydrogen evolution rate is also supported by photoluminance (PL) study. PL Study shows that there is a decrease in PL intensity in case of ZS-4 Sample which indicates many vacancy defects in the composites which ultimately inhibits charge carrier recombination. In nutshell, the nanoheterostructure, flower like morphology is responsible for good hydrogen evolution in case of ZS-4 Sample.

4 Conclusions

In nutshell, SiO_2@$ZnIn_2S_4$ nanoheterostructure with marigold flower like structure was synthesized successfully. The photocatalytic efficiency of the SiO_2@$ZnIn_2S_4$ nanoheterostructure for the evolution of hydrogen under natural sunlight was investigated. The highest H_2 evolution *i.e.* 796 μmol h^{-1} g^{-1} for water splitting & 6730 μmol h^{-1} g^{-1} for H_2S Splitting using 0.75 wt percent SiO_2 loading on $ZnIn_2S_4$ was achieved which is almost twice of pristine $ZnIn_2S_4$. It is due to high crystallinity, flower-like morphology and band structure of SiO_2@$ZnIn_2S_4$. This study highlights the nanoheterostructure with marigold flower like morphology which shows efficient charge separations due to intimate contact of the SiO_2 with nanopetals of flowers. Such kind of other nanoheterostructures may have potential as a photocatalyst for higher hydrogen evolution.

Conflicts of interest

There is no any conflict of intrest.

Acknowledgements

ARG like to thanks Dr R. J. Barnabas (Principal Ahmednagar College Ahmednagar) for useful suggestions and discussion and JRD Tata, SPPU for financial support. The authors would like to thank Nanocrystalline materials group. BBK would like to thanks the Ministry of Electronics and Information Technology (MeitY), Government of India and C-MET Pune for providing research facilities.

References

1 H. She, Y. Sun, S. Li, J. Huang, L. Wang, G. Zhu and Q. Wang, *Appl. Catal., B*, 2019, **245**, 439–447.
2 Y. A. Sethi, R. P. Panmand, S. R. Kadam, A. K. Kulkarni, S. K. Apte, S. D. Naik, N. Munirathnam, M. V. Kulkarni and B. B. Kale, Nanostructured CdS sensitized CdWO4 nanorods for hydrogen generation from hydrogen sulfide and dye degradation under sunlight, *J. Chem. Inf. Model.*, 2017, **487**, 504–512.
3 P. Kumar, R. Boukherroub and K. Shankar, Sunlight-driven water-splitting using twodimensional carbon based semiconductors, *J. Mater. Chem. A*, 2018, **6**, 12876–12931.
4 S. R. Kadam, S. W. Gosavi, B. B. Kale, N. Suzuki, C. Terashima and A. Fujishima, *Sci. Rep.*, 2019, **9**, 1–10.
5 A. K. Kulkarni, R. P. Panmand, Y. A. Sethi, S. R. Kadam, S. P. Tekale, G.-H. Baeg, A. V. Ghule and B. B. Kale, In situ preparation of N doped orthorhombic Nb2O5 nanoplates/rGO composites for photocatalytic hydrogen generation under sunlight, *Int. J. Hydrogen Energy*, 2018, **43**, 19873.
6 R. Singh and S. Dutta, A review on H2 production through photocatalytic reactionsusing TiO2/TiO2- assisted catalysts, *Fuel*, 2018, **220**, 607–620.
7 K. Fan, Z. Jin, G. Wang, H. Yang, D. Liu, H. Hu, G. Lu and Y. Bi, *Catal. Sci. Technol.*, 2018, **8**, 2352–2363.
8 F. Opoku, K. K. Govender, C. G. C. E. van Sittert and P. P. Govender, *New J. Chem.*, 2017, **41**, 11701–11713.
9 A. A. Dubale, A. G. Tamirat, H.-M. Chen, T. A. Berhe, C.-J. Pan, W.-N. Su and B.-J. Hwang, *J. Mater. Chem. A*, 2016, **4**, 2205–2216.
10 T. Su, Z. D. Hood, M. Naguib, L. Bai, Si Luo, C. M. Rouleau, I. N. Ivanov, H. Ji, Z. Qin and Z. Wu, *Nanoscale*, 2019, **11**, 8138–8149.
11 X. L. Ge, C. X. Li, Z. Q. Li and L. W. Yin, Tannic acid tuned metal-organic framework as a high-efficiency chemical anchor of polysulfide for lithium-sulfur batteries, *Electrochim. Acta*, 2018, **281**, 700–709.
12 E. A. Dolgopolova, A. M. Rice, C. R. Martin and N. B. Shustova, Photochemistry and photophysics of MOFs: steps towards MOF-based sensing enhancements, *Chem. Soc. Rev.*, 2018, **47**, 4710–4728.
13 F. C. Leng, H. Liu, M. L. Ding, Q. P. Lin and H. L. Jiang, Boosting photocatalytic hydrogen production of porphyrinic MOFs: the metal location in metalloporphyrin matters, *ACS Catal.*, 2018, **8**, 4583–4590.
14 S. Wang, B. Y. Guan and X. W. (David) Lou, Construction of ZnIn2S4-In2O3 hierarchical tubular heterostructures for

efficient CO2 photoreduction, *J. Am. Chem. Soc.*, 2018, **140**, 5037–5040.
15 B. Valizadeh, T. N. Nguyen, B. Smit and K. C. Stylianou, Porous metal-organic framework@polymer beads for iodine capture and recovery using a gas-sparged column, *Adv. Funct. Mater.*, 2018, **28**, 1801596–1801601.
16 W. Pudkon, S. Kaowphong, S. Pattisson, P. J. Miedziak, H. Bahruji, T. E. Davies, D. J. Morgan and G. J. Hutchings, *Catal. Sci. Technol.*, 2019, **9**, 5698–5711.
17 S. B. Kale, R. S. Kalubarme, M. A. Mahadadalkar, H. S. Jadhav, A. P. Bhirud, J. D. Ambekar, C.-J. Park and B. B. Kale, *Phys. Chem. Chem. Phys.*, 2015, **17**, 31850–31861.
18 Y. Xia, Q. Li, K. Lv, D. Tang and M. Li, *Appl. Catal., B*, 2017, **206**, 344–352.
19 D. Zeng, Z. Lu, X. Gao, B. Wu and W.-J. Ong, *Catal. Sci. Technol.*, 2019, **9**, 4010–4016.
20 Y. Gao, K. Qian, B. Xu, Fu Ding, V. Dragutan, I. Dragutan, Y. Sun and Z. Xu, *RSC Adv.*, 2020, **10**, 32652–32661.
21 A. R. Gunjal, A. K. Kulkarni, U. V. Kawade, Y. A. Sethi, R. S. Sonawane, J. Ook-Baeg, A. V. Nagawade and B. B. Kale, *Nanoscale Adv.*, 2020, **2**, 2577–2586.
22 Yu Gao, B. Xu, C. Mohamed, Yu He, Q. Zhang, F. Vidal, X. Wang, Fu Ding, Y. Sun, D. Ma, Y. Bi and Z. Xu, *Appl. Catal., B*, 2020, **279**, 119403.
23 W. Chen, R.-Q. Yan, J.-Q. Zhu, G.-Bo Huang and Z. Chen, *Appl. Surf. Sci.*, 2020, **504**, 144406.
24 K. Huang, C. Li and X. Meng, *J. Colloid Interface Sci.*, 2020, **580**, 669–680.
25 X. Zhao, W. Ju, J. Zhang, B. Liu, J. Zhang and X. Yi, *New J. Chem.*, 2019, **43**, 6234–6241.
26 F. Yuan, S. Pascale, J. Lakey, S. Riahi, A. T. McDonald, M. Shrestha, D. J. Tobias, M. Shiraiwa and V. H. Grassian, *Chem. Sci.*, 2019, **10**, 2906–2914.
27 J. Sun, H. Bi, S. Su, H. Jia, X. Xie and L. Sun, *J. Membr. Sci.*, 2018, **553**, 131–138.
28 H. Xu, J. Yan, Y. Xu, Y. Song, H. Li, J. Xia, C. Huan and H. Wan, *Appl. Catal., B*, 2017, **206**, 344–352.
29 H. Qiang, X. Niu, C. Nie, S. Hao, W. Zou, J. Ge, D. Chen and W. Yao, *Phys. Chem. Chem. Phys.*, 2016, **18**, 31410–31418.
30 L. Wang, H. Zhou, H. Zhang, H. Zhang, Y. Song, H. Zhang and X. Qian Inorg, *Chem*, 2020, **59**(4), 2278–2287.
31 W. Zhang, Y. Zhang, K. Yang, Y. Yang, J. Jia and L. Guo, *Nanomaterials*, 2019, **9**, 1671.
32 AshutoshKumar, M. Khan, X. Zen and I. M. C. Lo, *Chem. Eng. J.*, 2018, **353**, 645–656.
33 F. Wang, M. Li, L. Yu, F. Sun, Z. Wang, L. Zhang, H. Zeng and X. Xu, *Sci. Rep.*, 2017, **7**, 6960.
34 C. Liu, Y. Dong, J. Yang, T. Yao, Y. Wang and Z. Jiang, *ACS Appl. Mater. Interfaces*, 2013, **5**(9), 3824–3832.
35 R. M. Mohameda and F. A. Harraz, *Mater. Res. Bull.*, 2020, **131**, 110965.
36 X. Meng, Y. Zhuang, H. Tang and C. Lu, *J. Alloys Compd.*, 2018, **761**, 15–23.
37 X. Lin, X. Guo, D. Liu, Q. Wang, H. Zhai and L. Chang, *Mater. Res. Bull.*, 2015, **63**, 72–79.
38 K. Huang, C. Li and X. Meng, *J. Colloid Interface Sci.*, 2020, **580**, 669–680.
39 Y. Chen, S. Hu, W. Liu, X. Chen, L. Wu, X. Wang, P. Liu and Z. Li, *Dalton Trans.*, 2011, **40**, 2607–2613.
40 A. Khan, M. Danish, U. Alam, S. Zafar and M. Muneer, Facile Synthesis of a Z-Scheme ZnIn2S4/MoO3 Heterojunction with Enhanced Photocatalytic Activity under Visible Light Irradiation, *ACS Omega*, 2020, **5**(14), 8188–8199.
41 S. Lai, Z. Yang, J. Li, B. Shao, J. Yang, Y. Wang, J. Qiu and Z. Song, *J. Mater. Chem. C*, 2015, **3**, 7699–7708.
42 J. Wang, Y. Chen, W. Zhou, G. Tian, Y. Xiao, H. Fu and H. Fu, *J. Mater. Chem. A*, 2017, **5**, 8451–8460.
43 W. Pudkon, H. Bahruji, P. J. Miedziak, T. E. Davies, D. J. Morgan, S. Pattisson, S. Kaowphong and G. J. Hutchings, *Catal. Sci. Technol.*, 2020, **10**, 2838–2854.
44 M. Li, Y. Tao, J. Tang, Y. Wang, X. Zhang, Y. Tao and X. Wang, Synergetic Organocatalysis for Eliminating Epimerization in RingOpening Polymerizations Enables Synthesis of Stereoregular Isotactic Polyester, *J. Am. Chem. Soc.*, 2019, **141**, 281–289.
45 Y. Chen, G. Tian, W. Zhou, Y. Xiao, J. Wang, X. Zhang and H. Fu, *Nanoscale*, 2017, **9**, 5912–5921.
46 M. A. Mahadadalkar, S. B. Kale, R. S. Kalubarme, A. P. Bhirud, J. D. Ambekar, S. W. Gosavi, M. V. Kulkarni, C.-J. Park and B. B. Kale, *RSC Adv.*, 2016, **6**, 34724–34736.
47 Y. A. Sethia, A. K. Kulkarnib, A. A. Ambalkara, S. K. Khorea, A. R. Gunjala, S. W. Gosavi and B. B. Kale, *Nanoscale Adv.*, 2021, **3**, 508–516.
48 U. V. Kawade, R. P. Panmand, Y. A. Sethi, M. V. Kulkarni, S. K. Apte, S. D. Naik and B. B. Kale, *RSC Adv.*, 2014, **4**(90), 49295–49302.